Effect of shocklets on the velocity gradients in highly compressible isotropic turbulence

Jianchun Wang, Yipeng Shi, Lian-Ping Wang, Zuoli Xiao, Xiantu He et al.

Related Articles

Analytical and experimental study on the fluid structure interaction during air blast loading
J. Appl. Phys. 110, 114901 (2011)

Shock-wave solutions in two-layer channel flow. II. Linear and nonlinear stability
Phys. Fluids 23, 112101 (2011)

Experimental study of the hydrodynamic expansion following a nanosecond repetitively pulsed discharge in air
Appl. Phys. Lett. 99, 121502 (2011)

Regularized shock solutions in coating flows with small surface tension
Phys. Fluids 23, 093103 (2011)

On the evolution of spherical gas interfaces accelerated by a planar shock wave
Phys. Fluids 23, 084104 (2011)

Additional information on Phys. Fluids

Journal Homepage: http://pof.aip.org/

Journal Information: http://pof.aip.org/about/about_the_journal

Top downloads: http://pof.aip.org/features/most_downloaded

Information for Authors: http://pof.aip.org/authors

Effect of shocklets on the velocity gradients in highly compressible isotropic turbulence

Jianchun Wang,[1,a)] Yipeng Shi,[1] Lian-Ping Wang,[2] Zuoli Xiao,[1] Xiantu He,[1] and Shiyi Chen[1,a)]

[1]*State Key Laboratory of Turbulence and Complex Systems, Center for Applied Physics and Technology, College of Engineering, Peking University, Beijing 100871, People's Republic of China*
[2]*Department of Mechanical Engineering, University of Delaware, Newark, Delaware 19716, USA*

The effect of randomly generated shocklets on velocity gradients in a three-dimensional compressible isotropic turbulence was systematically studied. The forced flows obtained from high-resolution simulations had a turbulent Mach number of 1.0 and a Taylor microscale Reynolds number around 180. The shock detection algorithm developed by Samtaney *et al.* ["Direct numerical simulation of decaying compressible turbulence and shocklet statistics," Phys. Fluids **13**, 1415 (2001)] was applied to extract the shocklets. Using reference frames moving with the detected shocks, we obtained statistical properties of velocity and its gradients both upstream and downstream of the shocks. It was shown that the shocks induced flow modulation at a wide range of length scales, including the inertial subrange scales. The shocks intensified enstrophy in the shock regions and this enhanced enstrophy production was partially redistributed over various scales and dissipated by straining and viscous effects outside the shock regions. We also found that both the strain rate eigenvectors and eigenvalues were significantly altered by shocks. Furthermore, local modulation effects by the shocklets enlarged with the shocklet strength. The Helmholtz decomposition was performed to show that most statistics associated with the solenoidal component of velocity derivatives were insensitive to the formation of shocks, but those associated with the compressive component of velocity derivatives depended strongly on the shock formation and shock strength. © *2011 American Institute of Physics*. [doi:10.1063/1.3664124]

I. INTRODUCTION

The effect of compressibility on the structure and statistics of a turbulent flow is of fundamental importance to many applications such as the design of hypersonic aircraft, supersonic combustion, and inertial confinement fusion. A better physical understanding of compressible turbulence is desired in order to develop new turbulence models for compressible flows. In this work, we investigate systematically the effects of compressibility and shock discontinuities on the dynamics of small-scale flow features in a numerically simulated, well-resolved, highly compressible turbulence.

Compared to incompressible turbulence, there are stronger nonlinear couplings between the velocity field and thermal or temperature field in compressible turbulent flows; and such couplings have not been carefully considered in the modeling of highly compressible turbulence. The thermal field affects the density, pressure, and fluid viscosity, and, therefore, influences the local mass and momentum conservations. At the same time, the velocity field generates convective transport, pressure work, and local viscous heating affecting the evolution of the thermal field. Therefore, the dynamics is more complicated than the much well studied incompressible fluid turbulence.

Specifically, the occurrence of localized shocklets in the flow field at moderate to high turbulent Mach numbers is a manifestation of such strong coupling, leading to rapid conversion of kinetic energy into internal energy by dilatational dissipation and pressure work, as well as vorticity intensification by high local compression. Zeman[1] proposed a shocklet dissipation theory to quantify the dilatational dissipation in terms of turbulence energy, turbulent Mach number, and kurtosis of the velocity. His turbulence model incorporating the effect of dilatational dissipation successfully predicted the reduced growth rate of compressible mixing layers. Zeman[2] extended a second-order model of incompressible isotropic turbulence to the compressible regime by including contributions from the pressure dilatation and dilatational dissipation. Comparison with results from direct numerical simulations showed that the extended model well captured the effect of compressibility. In a systematic study of compressible homogeneous turbulence, Sarkar *et al.*[3] found that, at small and moderate Mach numbers, the compressive component of the flow was in dynamic quasi-equilibrium with respect to the incompressible component of the flow. A model for dilatational dissipation was proposed based on an asymptotic analysis at small turbulent Mach number. This model was capable of predicting the reduced growth rate of a compressible mixing layer.

Lee *et al.*[4] performed numerical simulations of decaying isotropic turbulence to demonstrate eddy shocklets in the three-dimensional compressible turbulence. Shocklets generated by

---
a)Authors to whom correspondence should be addressed. Electronic addresses: jwang.pku@gmail.com and syc@pku.edu.cn.

the fluctuating fields of turbulent eddies were found to have all characteristics of a typical shock wave. A strong correlation between pressure and dilatation was observed in the zones of eddy shocklets, leading to rapid conversion of kinetic energy into internal energy. Kida and Orszag[5] investigated the interaction between vorticity and shock waves by performing numerical simulations of decaying isotropic turbulence at initial root mean square (rms) Mach number up to 0.8. They showed that the baroclinic effect was relatively weak as density and pressure gradients were largely parallel. However, in the case of two distinct fluids, the baroclinic effect was pronounced at density interfaces.[6] They also showed that vorticity was enhanced by compression in the shock regions and, outside the shock regions, vortex stretching still dominated the generation of vorticity. Kida and Orszag[7,8] also analyzed energy transfer of solenoidal and compressive components of the velocity field in forced and decaying compressible isotropic turbulence. They found that coupling between two components of kinetic energy was rather weak, and the most kinetic energy transferred directly into internal energy by pressure-dilatation interaction and viscous dissipation.

Samtaney *et al.*[9] presented direct numerical simulations of compressible isotropic turbulence at several turbulent Mach numbers (M_t) from 0.1 to 0.5. They developed a shocklet detection algorithm to extract shocklets from the simulated flows. The capability of this algorithm to detect shocklet surfaces was verified partially by comparing the relation between pressure and density changes across the detected shocks, to the ideal Rankine-Hugoniot jump condition. Using this detection algorithm, they analyzed the distribution of shocklet strength in the simulated flows. They also proposed a simple probability density function (PDF) model for the shocklet strength, which was in satisfactory agreement with the numerical simulation results. Pirozzoli and Grasso[10] carried out direct numerical simulations of decaying compressible isotropic turbulence at various values of initial turbulent Mach number (up to 0.8). The effect of compressibility on the time evolution of turbulence properties was studied. Dynamics of small-scale turbulent structures were analyzed and were compared with those in an incompressible turbulence. They found that the shocklets contributed significantly to the total dilatational dissipation. Lee *et al.*[11] studied the effect of compressibility on the turbulent velocity gradients at various turbulent Mach numbers (0.059 to 0.885). The behavior of velocity gradients conditioned on the local dilatation level was examined, showing a strong dependence of strain rate eigenvalues on the local dilatation. The preferential alignment between vorticity and strain rate eigenvectors found for incompressible turbulence was shown to be weakened by strong flow dilatation.

When simulating a highly compressible turbulence, a numerical method must resolve small-scale turbulent fluctuations with controlled and negligible numerical dissipation, while at the same time, provide a sufficient dissipation within the shock regions to capture shock waves without numerical instability. To address these two contradictory requirements, Adams and Shariff[15] first proposed a hybrid scheme combining a spectral-like compact finite difference (FD) scheme[12] and shock-capture WENO (weighted essentially non-oscillatory or

ENO) scheme.[13,14] They used a hybrid compact upwind FD-ENO scheme to treat the advection term and applied their method to study shock-turbulence interactions in one and two spatial dimensions. Later, Pirozzoli[16] developed a conservation formulation of hybrid scheme combining compact upwind FD and WENO and applied his method to study the interaction of a plan shock wave with 3D isotropic turbulence. The switch between compact upwind FD and WENO at the interface was further improved by introducing several complex weight functions (e.g., Ren *et al.*,[17] Zhou *et al.*[18]). In all these hybrid methods, the shock-detection method was based on differences of the solution variable at two adjacent grid points, which has the potential risk of treating strong small-scale turbulent fluctuations as shocks. Larsson *et al.*[19] applied a hybrid approach combining high-order central difference and WENO to simulate decaying compressible isotropic turbulence and found that the hybrid scheme performed much better than purely WENO scheme. Their shock detection was based on the local dilatation and vorticity, which was more accurate than previous methods. Recently, we[21] developed a novel hybrid method suitable for simulating highly compressible isotropic turbulence. Our hybrid scheme combines a 7th-order WENO scheme[20] for shocklet regions and an 8th-order compact central finite difference scheme[12] for smooth regions outside shocklets. A flux-based conservative and formally consistent formulation is implemented to optimize the treatment at the interface between the shocklet regions and the smooth regions, which also improves the computational efficiency. In addition, a novel numerical hyperviscosity formulation is proposed within the context of compact finite difference scheme for the smooth regions to improve numerical stability of the hybrid method. With these improvements, our new hybrid method was able to simulate compressible flows at higher turbulent Mach number.

In this paper, we present a systematic study of the effects of shocklets on statistical properties of velocity gradients, using a forced compressible turbulence with a turbulent Mach number of 1.03 simulated by a novel method that we developed recently.[21] This turbulent Mach number is higher than most of the previous studies. We apply the shock detection algorithm of Samtaney *et al.*[9] to extract shocklets from the turbulent flow. Several techniques such as the Helmholtz decomposition and conditional averages on the local shock strength are used to delineate the statistical significance of shocklets on a variety of average flow properties. In Sec. II, we describe briefly the physical governing equations, the simulation method, and parameters of the simulated highly compressible turbulent flow. The statistical properties of the detected shocklets in our flow will be described in Sec. III A, where we also demonstrate that local conservation laws for normal shock waves well describe the property changes across shocklets. Ensemble-average statistics of velocity and vorticity, in a reference frame moving with a shocklet, are reported in Sec. III B, in order to gauge the impact of shocklets on both local and global flow statistics. In Sec. III C, we examine the effect of shocklets on various terms in the enstrophy equation. The properties of strain rate tensors on the two sides of the shocklets are discussed in Sec. III D. Finally, Sec. IV contains a summary and main conclusions of our study.

II. GOVERNING EQUATIONS AND SYSTEM PARAMETERS

We consider a stationary compressible turbulence of an ideal gas driven and maintained by large-scale momentum forcing and thermal forcing. The kinetic energy cascade from large to small scales requires energy input through forcing at the large scales, to balance the viscous dissipation at the small scales. At the same time, the viscous dissipation is converted to thermal energy or heating at the small scales, and therefore, thermal energy must be removed by large-scale forcing. Following Samtaney et al.,[9] the governing equations of the compressible flow system, in dimensionless form, are written as

$$\frac{\partial \rho}{\partial t} + \frac{\partial (\rho u_j)}{\partial x_j} = 0, \tag{1}$$

$$\frac{\partial (\rho u_i)}{\partial t} + \frac{\partial [\rho u_i u_j + p\delta_{ij}/\gamma M^2]}{\partial x_j} = \frac{1}{\mathrm{Re}}\frac{\partial \sigma_{ij}}{\partial x_j} + \mathcal{F}_i, \tag{2}$$

$$\frac{\partial \mathcal{E}}{\partial t} + \frac{\partial [(\mathcal{E} + p/\gamma M^2)u_j]}{\partial x_j} = \frac{1}{\alpha}\frac{\partial}{\partial x_j}\left(\kappa \frac{\partial T}{\partial x_j}\right)$$
$$+ \frac{1}{\mathrm{Re}}\frac{\partial (\sigma_{ij} u_i)}{\partial x_j} - \Lambda + \mathcal{F}_j u_j, \tag{3}$$

$$p = \rho T, \tag{4}$$

where viscous stress σ_{ij} and total energy (internal plus kinetic energy) per unit volume $\mathcal{E}$ are

$$\sigma_{ij} = \mu\left(\frac{\partial u_i}{\partial x_j} + \frac{\partial u_j}{\partial x_i}\right) - \frac{2}{3}\mu\theta\delta_{ij}, \tag{5}$$

$$\mathcal{E} = \frac{p}{(\gamma - 1)\gamma M^2} + \frac{1}{2}\rho(u_j u_j). \tag{6}$$

Here, $\theta \equiv \partial u_k/\partial x_k$ is the normalized velocity divergence or dilatation, $\mathcal{F}_i$ is the dimensionless, divergence-free large-scale forcing per unit volume to the fluid momentum, and Λ is the dimensionless large-scale heat sink or cooling function per unit volume. In writing the above governing equations, we have used a reference length L, velocity U, density ρ_0, temperature T_0, speed of sound $c_0 \equiv \sqrt{\gamma R T_0}$, energy per unit volume $\rho_0 U^2$, pressure $\rho_0 R T_0$, viscosity μ_0, and thermal conductivity κ_0 to normalize the respective quantities. Here, $\gamma \equiv C_p/C_v$ is the ratio of specific heat at constant pressure C_p to that at constant volume C_v and is assumed to be equal to 1.4, and R is the specific gas constant. The three reference governing parameters are: the reference Prandtl number $\mathrm{Pr} \equiv \mu_0 C_p/\kappa_0$, the reference Reynolds number $\mathrm{Re} \equiv \rho_0 U L/\mu_0$, and the reference Mach number $M = U/c_0$. In this study, Pr is set to 0.7. The parameter α is defined as $\alpha \equiv \mathrm{Pr}\,\mathrm{Re}\,(\gamma-1)M^2$.

We employ the Sutherland's law to specify the temperature-dependent viscosity and thermal conductivity. In dimensionless form, they are[21]

$$\mu = \frac{1.4042 T^{1.5}}{T + 0.40417}, \tag{7}$$

$$\kappa = \frac{1.4042 T^{1.5}}{T + 0.40417}. \tag{8}$$

The velocity field is forced by fixing the kinetic energy per unit mass within the two lowest wavenumber shells, to prescribed values consistent with the $k^{-5/3}$ kinetic energy spectrum. The forcing field is divergence-free, as such it does not impact the large-scale divergence field.[21] In addition, a uniform thermal cooling $\Lambda = \langle \mathcal{F}_j u_j \rangle$ is added to the energy equation to prevent the internal energy from increasing.[21]

The system is characterized by two important parameters, namely, the Taylor microscale Reynolds number Re_λ and the turbulent Mach number M_t. They are defined as follows:[9]

$$\mathrm{Re}_\lambda = \mathrm{Re}\,\frac{\langle (u_1^2 + u_2^2 + u_3^2)/3 \rangle^{1/2} \lambda \langle \rho \rangle}{\langle \mu \rangle},$$
$$M_t = M\,\frac{\langle (u_1^2 + u_2^2 + u_3^2) \rangle^{1/2}}{\langle \sqrt{T} \rangle}, \tag{9}$$

where the normalized Taylor microscale λ is defined as

$$\lambda = \sqrt{\frac{\langle (u_1^2 + u_2^2 + u_3^2)/3 \rangle}{\langle [(\partial u_1/\partial x_1)^2 + (\partial u_2/\partial x_2)^2 + (\partial u_3/\partial x_3)^2]/3 \rangle}}. \tag{10}$$

The system is solved in a cubic box with periodic boundary condition in all three spatial directions. A novel hybrid numerical scheme with built-in hyperviscosity has been used to achieve both accuracy and numerical stability in the simulations. The hybrid scheme utilizes a 7th-order WENO scheme[20] for shocklet regions and an 8th-order compact central finite difference scheme[12] for smooth regions outside shocklets. A flux-based conservative and formally consistent formulation is implemented to optimize the treatment at the interface between the shocklet regions and the smooth regions and to improve the computational efficiency. The implementation details have been described in Wang et al.[21]

Three grid resolutions (256^3, 384^3, and 512^3) were considered in order to assess any dependence of small-scale flow statistics on the grid resolution. After reaching the statistically stationary state, a total of 27 flow fields covering the time period of $6.0 \le t/T_e \le 10.8$ was used to obtain statistical averages of interested quantities, where T_e is the large eddy turnover time. By setting $M = 0.45$ and $\mathrm{Re} = 500$, we obtained an average turbulent Mach number around $M_t = 1.0$ and Taylor microscale Reynolds number around $\mathrm{Re}_\lambda = 180$ for all simulations.

Other parameters and statistics of the simulation flows are compiled in Table I for all simulations. The resolution parameter $k_{max}\eta$ are, respectively, 1.38, 2.03, and 2.77, where Kolmogorov length scale $\eta = [(\langle \mu/(\mathrm{Re}\rho) \rangle)^3/\epsilon]^{1/4}$ are all around 0.011 and the largest wavenumber k_{max} are, respectively, 128, 192, and 256. The statistics shown in Table I imply that the small-scale flow is well resolved in the 384^3 and 512^3 simulations. In the definition of Kolmogorov length scale, the viscous dissipation $\epsilon = \langle \sigma_{ij} S_{ij}/\mathrm{Re} \rangle$ is used. The integral length scale L_f is computed by

TABLE I. Simulation parameters and resulting flow statistics.

Resolution	Re_λ	M_t	$k_{max}\eta$	L_f	L_f/η	u'	$u^{c'}/u^{s'}$	θ'	θ'/ω'	S_3
256^3	187	1.04	1.38	1.48	137	2.3	0.20	5.3	0.33	−1.1
384^3	175	1.05	2.03	1.46	138	2.2	0.22	6.0	0.37	−1.6
512^3	177	1.03	2.77	1.47	136	2.2	0.22	6.3	0.39	−1.9

$$L_f = \frac{3\pi}{4} \frac{\int_0^\infty [E(k)/k]dk}{\int_0^\infty E(k)dk},$$

where $E(k)$ is the energy spectrum at wavenumber k. For the given grid resolutions, there are roughly two decades of scale range between the integral length scale and the viscous scale. The velocity-derivative skewness is defined as

$$S_3 = \frac{[\langle(\partial u_1/\partial x_1)^3 + (\partial u_2/\partial x_2)^3 + (\partial u_3/\partial x_3)^3\rangle]/3}{\{[\langle(\partial u_1/\partial x_1)^2 + (\partial u_2/\partial x_2)^2 + (\partial u_3/\partial x_3)^2\rangle]/3\}^{3/2}},$$

$S_3 = -1.1$, -1.6, and -1.9 in our simulations; these are much larger than the typical value of -0.4 to -0.5 found in the incompressible turbulence. The deviation is caused by the frequent formations of shocklets in the compressible turbulence. The rms fluctuations of velocity, vorticity, and dilatation are also presented, where $u' = \langle u_1^2 + u_2^2 + u_3^2\rangle^{1/2}$ and $\omega' = \langle\omega_1^2 + \omega_2^2 + \omega_3^2\rangle^{1/2}$.

In summary, the overall statistical properties of the simulated flows at 512^3 grid resolution are well converged (except for the velocity-derivative skewness, which is most sensitive to the grid refinement). Further details on grid dependence will be provided later in the paper. If not specially indicated, the results shown in the rest of the paper are based on the 512^3 flow simulation.

To help clarify the underlying physics in the compressible turbulence and specifically the effects of compressibility, we employ the well-known Helmholtz decomposition[9] to the velocity field

$$\mathbf{u} = \mathbf{u}^s + \mathbf{u}^c, \tag{11}$$

where the solenoidal component $\mathbf{u}^s$ satisfies $\nabla \cdot \mathbf{u}^s = 0$, and the compressive component $\mathbf{u}^c$ is irrotational, i.e., $\nabla \times \mathbf{u}^c = 0$. In our simulations, we find that the average ratio of the rms fluctuations of the two components, $u^{c'}/u^{s'}$ is equal to 0.22, implying that the compressible component contributes to a
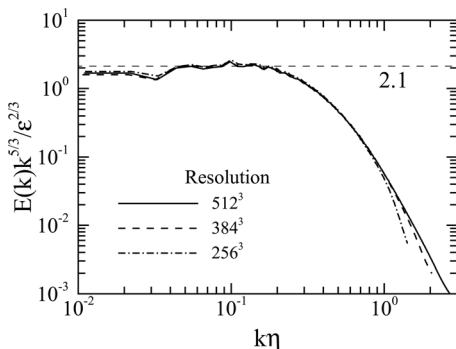

FIG. 1. Compensated kinetic energy spectra of the velocity field for three grid resolutions.
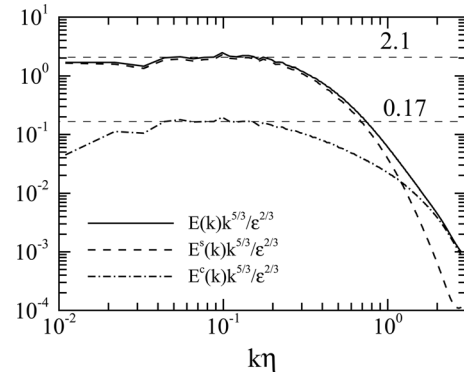

FIG. 2. Compensated kinetic energy spectra for the velocity field and its decomposed components.

small but finite fraction of the total kinetic energy. The ratio θ'/ω' (see Table I) is substantially larger than $u^{c'}/u^{s'}$, indicating that the compressive component of flow is more significant at the small scales.

In Fig. 1, we plot the compensated kinetic energy spectra for the velocity field $\mathbf{u}$ from all resolutions. The energy spectra from 384^3 and 512^3 resolutions overlap in almost all scale ranges, implying the convergence of energy spectra under this grid refinement. In addition, a short inertial range is identified, with a Kolmogorov constant of about 2.1 which is slightly higher than the values (1.5 to 2.0) typically observed for incompressible turbulent flows.[22] In Fig. 2, we plot the compensated kinetic energy spectra for the velocity field $\mathbf{u}$ and its two components $\mathbf{u}^s$ and $\mathbf{u}^c$. The energy spectra for $\mathbf{u}$ and $\mathbf{u}^s$ almost overlap except at high wavenumbers where the compressive component dominates the energy content.

In Figs. 3 and 4, we plot PDFs of normalized vorticity and velocity divergence for three grid resolutions. The PDFs of vorticity for 384^3 and 512^3 resolutions overlap almost everywhere. The PDFs of velocity divergence for 384^3 and 512^3 resolutions overlap exactly in expansion regions ($\theta > 0$) and have a slight difference in strong compression regions ($\theta/\theta' < -2$). Therefore, the PDF of velocity divergence is well resolved at 512^3 resolution.

III. EFFECT OF SHOCKLETS ON THE VELOCITY GRADIENTS

A. Statistics of shocklets

We begin with a discussion of the statistics of shocklets in the simulated turbulent flow. The PDF of the local Mach
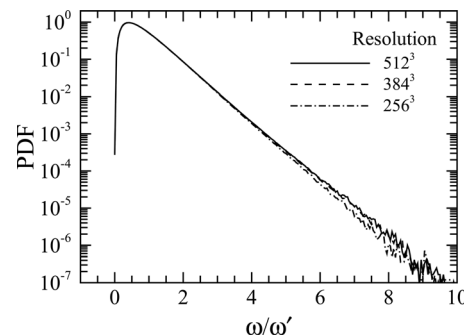

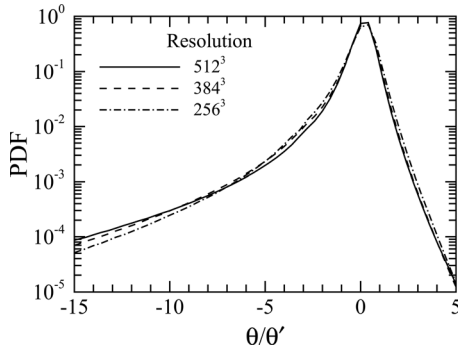FIG. 3. PDFs of normalized vorticity for three grid resolutions.

FIG. 4. PDFs of normalized velocity divergence for three grid resolutions.

FIG. 6. PDF of shock strength as measured by $M_n - 1$. Dashed line: $\beta_1 \exp[-\beta_2(M_n - 1)]$ with $\beta_1 = 1.2$ and $\beta_2 = 5.1$.

number $M_{loc} = M\sqrt{u_1^2 + u_2^2 + u_3^2}/\sqrt{T}$ is shown in Fig. 5. Clearly, a substantial portion of flow field is supersonic. The highest local Mach number exceeds 3.0. Therefore, in this flow field, there are shocklets generated by turbulent fluctuations at different scales and these are distributed randomly in space, see the dilatation contour plot, Fig. 14 in Wang *et al.*[21]

Samtaney *et al.*[9] developed a shocklet detection algorithm to display the shocklets in 3D compressible turbulence. They defined the regions occupied by the shocklets as

$$S = \{S_l | \nabla^2 \rho = 0, \theta < -3\theta'\}, \tag{12}$$

namely, the surface elements where the density exhibits inflection along the local normal and the compression rate is strong. The detailed extraction algorithm based on an edge-detection technique is described in Samtaney *et al.*[9]

Using the detected shocklets, a more precise representation of the shock strength is the normal upstream shock Mach number M_n in a reference frame moving with the shock, where M_n was estimated by using the shock relation

$$M_n = M\frac{u_{1n}}{\sqrt{T_1}} = \sqrt{\frac{\gamma + 1}{2\gamma}\frac{p_2}{p_1} + \frac{\gamma - 1}{2\gamma}}, \tag{13}$$

where u_{1n} is the normalized velocity, projected along the shock normal direction, upstream of a shocklet relative to the shocklet front. The normal direction of a shocklet is along the density gradient vector and points to the side of smaller density. Variables upstream of shocks (lower density side) are named with subscript 1 and downstream (higher
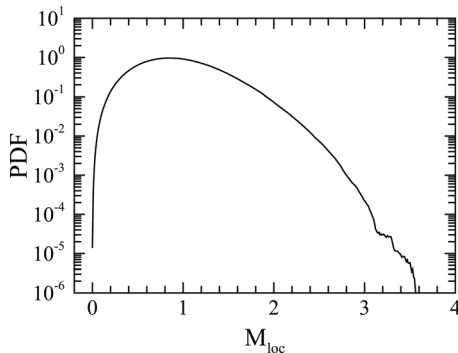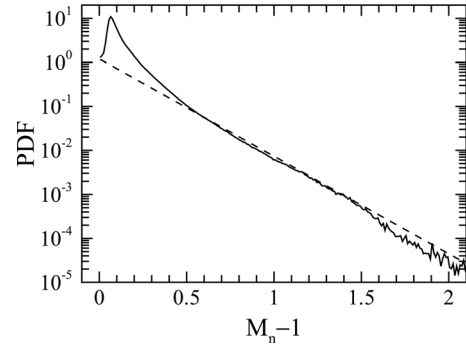
density side) variables with subscript 2. Therefore, the density ratio $\rho_r = \rho_2/\rho_1 > 1$ and the pressure ratio $p_r = p_2/p_1 > 1$ across shocks.

Fig. 6 shows the PDF of $M_n - 1$. There is a clear peak at $M_n - 1 \approx 0.07$, corresponding to the most probable pressure ratio $p_r = 1.17$. A wide distribution of M_n is observed, with a maximum M_n being larger than 3. This highly intermittent distribution of shock strength is demonstrated by an exponential tail in the PDF, which can be fitted by $P(M_n - 1) = \beta_1 \exp[-\beta_2(M_n - 1)]$ with $\beta_1 = 1.2$ and $\beta_2 = 5.1$. This exponential tail differs from the theoretical prediction by Samtaney *et al.*[9] who proposed a super-exponential description as $P(M_n - 1) = 2\beta^*(M_n - 1)\exp[-\beta^*(M_n - 1)^2]$. Their theory was based on the assumption of weak shocks. The turbulent Mach numbers in our simulations are higher than those realized in their simulations. The moderate and strong shocks found in our simulated flows deviate significantly from their weak-shock prediction.

The Rankine-Hugoniot jump condition relates the density ratio with the pressure ratio across a shock front and is written as

$$\rho_r = \frac{(\gamma + 1)p_r + \gamma - 1}{(\gamma - 1)p_r + \gamma + 1}. \tag{14}$$

In Fig. 7, we plot the density ratios against the corresponding pressure ratios across shocks obtained from our simulated flows. A total of 5000 pairs (shown as small open squares) of these ratios for detected shocks are shown. The line shows ideal Rankine-Hugoniot relation. Most points lie very close

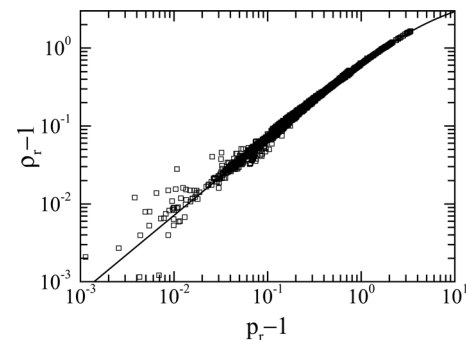FIG. 5. PDF of the local Mach number.

FIG. 7. Density ratio vs pressure ratio across the detected shocklets. 5000 points are used in the plot. The solid curve is the Rankine-Hugoniot relation.

to the ideal curve and about 8.5% of the total points fail to satisfy the jump condition within a tolerance of $C_t = 10\%$, where the tolerance is defined as

$$C_t = \frac{1}{\rho_r - 1}\left|\rho_r - \frac{(\gamma+1)p_r + \gamma - 1}{(\gamma-1)p_r + \gamma + 1}\right|.$$

The deviation from the ideal curve becomes more obvious at small density ratios as expected, since for weak shocks, the effect of viscosity is pronounced, breaking the inviscid condition of ideal shock. The curvature of the shocklets can also modify the ideal relation.[23]

Fig. 8 displays the PDF of C_t and the average of C_t conditioned on M_n. Clearly, the average C_t decreases rapidly with increasing M_n when $1.0 < M_n < 1.5$. The average tolerance stays below 1% when $M_n \geq 1.5$. The fraction of detected shocks with $M_n > 1.1$ is estimated as 43.2%, where only about 1.7% of the total points fail to satisfy the jump condition within a tolerance of $C_t = 10\%$. These statistics demonstrate that the dynamics of most moderate and strong shocks are governed by local conservation laws across the shocks and the local normal shock relations become increasingly more accurate as the shock strength is increased.

To further verify the shock jump condition, we interpolate the normal velocity increments across shocks from the velocity field. The change in the normal velocity across an idealized shock can be written as

$$|u_{2n} - u_{1n}| = \sqrt{\frac{2(p_2 - p_1)^2}{\rho_1[(\gamma+1)p_2 + (\gamma-1)p_1]}}. \quad (15)$$

Fig. 9 shows that this ideal jump condition fits quite well to the measured velocity jumps in our simulations. The deviations from the ideal value are typically within $u'/10$ (Only 2.1% of points fall outside of $u'/10$ deviations). We observe that the strongest velocity jump is comparable to the level of velocity fluctuations ($u' = 2.20$, see Table I) in the turbulence. This implies that there is a significant effect of shocks on the statistical properties of the velocity field.

B. Effect of shocklets on the velocity and vorticity field

The phenomenon of shock-turbulence interaction in the isotropic turbulence is more complicated than the canonical
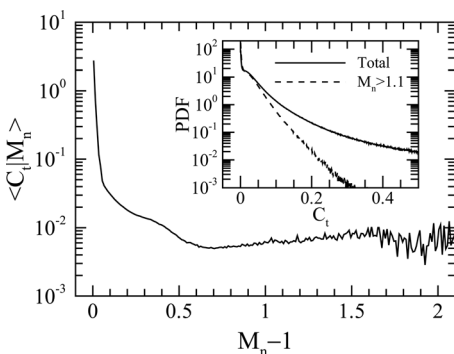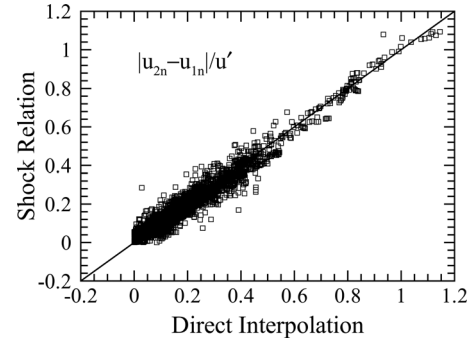

FIG. 9. Comparison of normal velocity increments across the shocks computed with the ideal relation and values obtained in the simulation. 5000 points are used in the plot.

shock-turbulence interaction[23–26] since the spatial distribution, sizes, and shapes of shocks here are quite random. In addition, treating the shock waves as an added type of coherent structure, there are mutual interactions that affect the long-range correlations of relevant variables. The shock detect algorithm provides a collection of shock waves in the isotropic turbulence. By using this collected database, we can explore the statistics of turbulence upstream and downstream of a shock in the reference frame moving with the shock.

In the local reference frame moving with a shock, we use d to indicate the normal distance from the shock surface. d is assumed to be positive upstream of the shock and negative downstream of the shock. We denote $\langle f \rangle^{(d)}$ as the ensemble average of a variable f along the normal direction, averaged over a large number of shocks.

In Fig. 10, we plot the average dilatation relative to the shock front. It is observed that there is a strong compression region at the shock front, accompanied by an extended expansion region downstream of the shock. A similar phenomenon was reported by Larsson and Lele,[26] who examined the instantaneous structure of the shock-turbulence interaction conditioned on the shock strength. They found that in the strong shock region, the flow is characterized by overcompression, followed by an expansion. In Fig. 11, we plot the average dilatation relative to the shock front conditioned on the shock strength. As the shock strength grows, the maximum compression becomes stronger inside the shock, and the expansion downstream of the shock is also amplified.
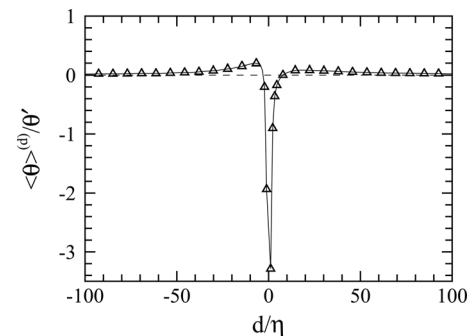

FIG. 8. The average tolerance C_t conditioned on the normal upstream shock Mach number M_n. Inset: the PDF and conditional PDF of C_t.

FIG. 10. The variation of average dilatation as a function of distance from the shock front. Positive d for the upstream and negative d for the downstream locations.
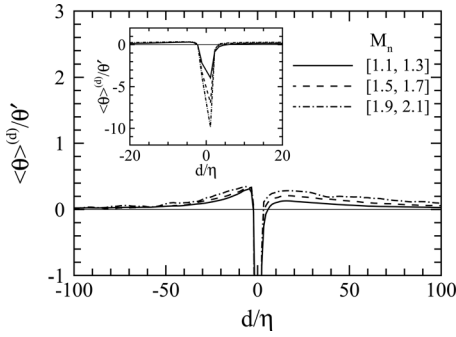
FIG. 11. The variation of average dilatation as a function of distance from the shock front conditioned on the shock strength.

FIG. 13. The variation of average normal velocity as a function of distance from the shock front for three types of grid resolutions.

Furthermore, the average dilatation is always positive upstream of the strong shocks, which is different from the canonical shock-turbulence interaction,[26] where the average upstream dilatation is almost zero.

The average normal velocity u_n and tangential vorticity ω_t on two sides of shocks are shown in Fig. 12, where $u_n = \boldsymbol{u} \cdot \boldsymbol{n}$ and $\omega_t = |\boldsymbol{\omega} - (\boldsymbol{\omega} \cdot \boldsymbol{n})\boldsymbol{n}|$. The downstream normal velocity is roughly 50% less than the upstream value, as a substantial amount of the kinetic energy is transferred to the internal energy across the shocks. In contrast, the tangential vorticity downstream is amplified by 50% relative to the upstream value, in agreement with the result in the canonical shock-turbulence interaction.[26] The relative differences of tangential vorticity on two sides of the shocks remain significant at $d = \pm 50\eta$, where η is the Kolmogorov length scale. This scale is well within the inertial range, implying a long-range effect of shock waves on the turbulent flow, despite that the shock thickness is typically smaller than the inertial scale. It is important to note that the typical length of the shock fronts falls in the inertial subrange and in some cases, even comparable to the integral length scale of the flow, e.g., see the dilatation contour plot, Fig. 14 in Wang et al.[21]

In Fig. 13, we plot the average normal velocity distributions on two sides of the shocks for three grid resolutions. Although there are some differences of upstream normal velocity under these resolutions, the difference between 384^3 and 512^3 grid resolutions is negligible. In Fig. 14, the average tangential vorticity distributions on two sides of the shocks for three grid resolutions are shown. It is found that tangential vorticity is more sensitive to change in grid
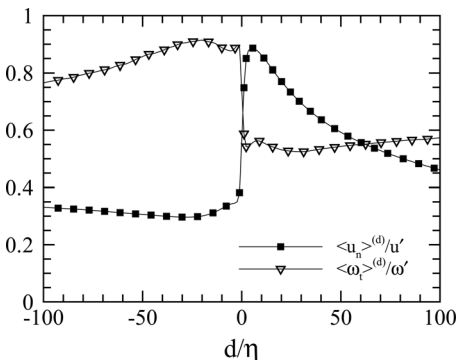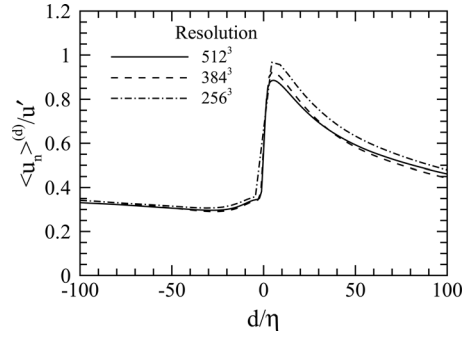
resolution than the normal velocity. The curve of the average tangential vorticity near shocks at 256^3 grid resolution substantially deviates from these of higher grid resolutions. Both 384^3 and 512^3 grid resolutions capture main features of the average tangential vorticity near shocks: abrupt jump across the shocks with amplification by 50% relative to the upstream value and decay slowly after.

In Fig. 15, we plot the average normal velocity on two sides of the shocks conditioned on the shock strength. Larger upstream normal velocity is required for the formation of the stronger shock while the average normal velocity downstream of the shock remains nearly the same as the shock strength increases. In Fig. 16, the average tangential vorticity on two sides of the shocks conditioned on the shock strength is shown. A similar feature is revealed: the statistics downstream of shock is insensitive to the shock strength. On the other hand, the average upstream tangential vorticity is weakened by a larger magnitude as the shock strength is increased.

The alignments of velocity and vorticity vectors relative to the shock normal are shown in Fig. 17. A perfect alignment corresponds to a value of one, and a random alignment would give a value of 0.5 for $\langle|\cos(\text{angle})|\rangle$ (averaged over a spherical view-angle surface). Substantial deviations from the random alignment are observed for the velocity upstream of the shocks and for the vorticity downstream of the shocks. It is interesting to see the more coherent alignment of velocity upstream of the shocks, indicating that generation of shock waves is a non-local phenomenon in the isotropic turbulence. Figs. 18 and 19 show PDFs of cosines of angles between the shock normal and velocity or vorticity at a few

FIG. 12. Variations of average normal velocity and tangential vorticity as a function of distance from the shock front.
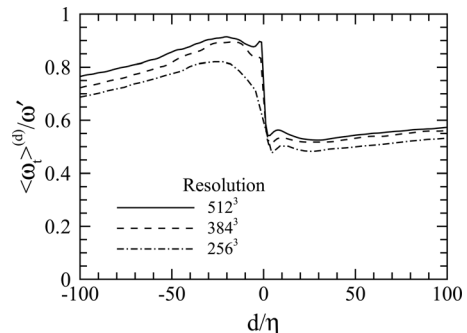

FIG. 14. The variation of average tangential vorticity as a function of distance from the shock front for three types of grid resolutions.
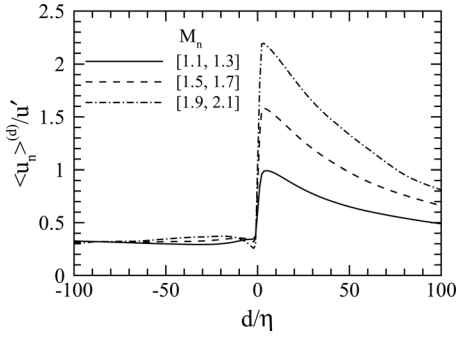
FIG. 15. The variation of average normal velocity as a function of distance from the shock front conditioned on the shock strength.

selected distances from the shock front. The anti-parallel alignment between upstream velocity and shock normal is weakened gradually as the sample point shifts away from shock. Due to the tangential vorticity jump across shocks,[26] there is a strong tendency for the downstream vorticity to align perpendicularly to the shock normal direction. The perpendicular alignment remains significant even at $d = -72\eta$ ($k = -64$), indicating that the vorticity production by shocks is rather significant and its effect on the flow extends over a wide range of scales.

C. Effect of shocklets on the enstrophy generation

The enstrophy is governed by the following evolution equation:[27]

$$\left(\frac{\partial}{\partial t} + u_j \frac{\partial}{\partial x_j}\right)\frac{\omega^2}{2} = \omega_i \omega_j S_{ij}^s + \omega_i \omega_j S_{ij}^{c*} - \frac{2}{3}\theta\omega^2$$
$$+ \omega_i \frac{\epsilon_{ijk}}{\gamma M^2}\frac{1}{\rho^2}\frac{\partial\rho}{\partial x_j}\frac{\partial p}{\partial x_k} + \omega_i \frac{\epsilon_{ijk}}{Re}\frac{\partial}{\partial x_j}\left(\frac{1}{\rho}\frac{\partial\sigma_{mk}}{\partial x_m}\right). \tag{16}$$

We denote the straining term $W_s = \omega_i \omega_j S_{ij}^* = \omega_i \omega_j S_{ij}^s + \omega_i \omega_j S_{ij}^{c*}$, the dilatation term $W_d = -\frac{2}{3}\theta\omega^2$, the baroclinic term $W_b = \omega_i \frac{\epsilon_{ijk}}{\gamma M^2}\frac{1}{\rho^2}\frac{\partial\rho}{\partial x_j}\frac{\partial p}{\partial x_k}$, and the viscous term $W_v = \omega_i \frac{\epsilon_{ijk}}{Re}\frac{\partial}{\partial x_j}\left(\frac{1}{\rho}\frac{\partial\sigma_{mk}}{\partial x_m}\right)$. Note that S_{ij}^* is the anisotropic part of the strain rate tensor S_{ij}, and S_{ij}^s and S_{ij}^{c*} are, respectively, the solenoidal component and compressive

component of S_{ij}^*, i.e., $S_{ij}^s = (\partial u_i^s/\partial x_j + \partial u_j^s/\partial x_i)/2$ and $S_{ij}^{c*} = (\partial u_i^c/\partial x_j + \partial u_j^c/\partial x_i)/2 - \theta\delta_{ij}/3$.

Averages of these terms on two sides of shocks are plotted in Fig. 20. All terms are already normalized by the average enstrophy production $\langle W_s \rangle$. Due to a strong correlation between density and pressure field, the baroclinic term is always negligible, in agreement with the result in Kida and Orszag.[5] In the shock region, dilatation term dominates the generation of enstrophy. Thus, the enstrophy jump across shocks ascribes to the effect of strong compression. Dilatation term also causes some destruction of enstrophy in the expansion region downstream of shocks. In the shock free region, straining term makes the main contribution to the production of enstrophy, indicating that, as in an incompressible turbulence, vortex stretching is the dominant mechanism for enstrophy production there, similar to results shown in Kida and Orszag.[5]

Another important observation is that the sum of the terms is slightly negative outside the shock region, but is highly positive within the shock region. The net spatial average of the sum must be zero. This implies that the additional enstrophy produced inside the shocks by compression is partially advected, transferred across scales, and dissipated outside the shocks.

In Fig. 21, averages of two components of the straining term, $W_s^s = \omega_i W_i^s$ and $W_s^c = \omega_i W_i^c$, on two sides of shocks are shown. It is observed that there is a clear peak of the straining term inside shocks due to its compressive component, while

FIG. 17. Average cosines of the angles between the shock normal and velocity or vorticity direction on two sides of shocks.
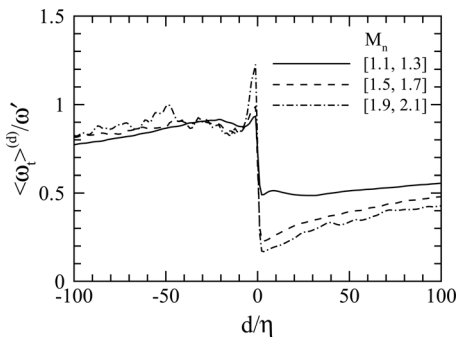

FIG. 16. The variation of average tangential vorticity as a function of distance from the shock front conditioned on the shock strength.

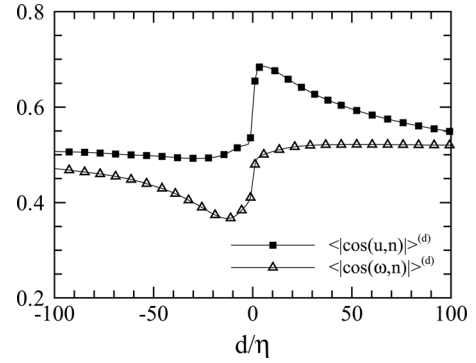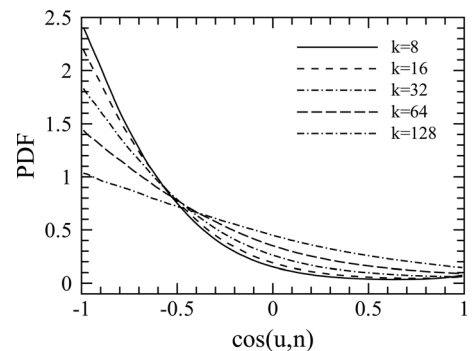FIG. 18. PDFs of cosines of angles between the shock normal and velocity upstream of shocks. The sample points are located k grid points away from the shock front and $d/\eta = 1.12 k$.
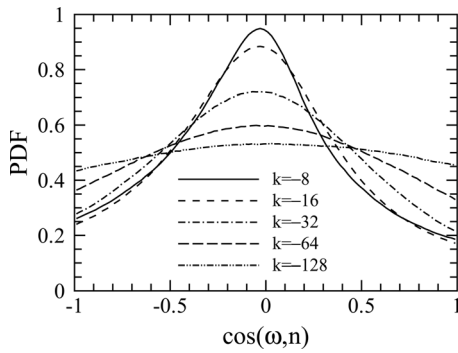
FIG. 19. PDFs of cosines of angles between the shock normal and vorticity downstream of the shocks. The sample points are located k grid points away from the shock front and $d/\eta = 1.12 \, k$.

FIG. 21. Average straining terms on two sides of the shocks according to the Helmholtz decomposition.

the solenoidal component of the straining term varies smoothly across shocks. Downstream of the shocks, expansion leads to a slight reduction of enstrophy by the compressive straining term. Therefore, the role of compressive straining term on the enstrophy dynamics is quite similar to that of the dilatation term, but with a magnitude much smaller than that of the dilatation term.

Fig. 22 shows average cosines of angles between vorticity and the vortex stretching vectors $W_i = \omega_j S_{ij}^*$, $W_i^s = \omega_j S_{ij}^s$, and $W_i^c = \omega_j S_{ij}^{c*}$. The positive values of $\langle \cos(\omega, \, \boldsymbol{W}) \rangle^{(d)}$ and $\langle \cos(\omega, \, \boldsymbol{W}^s) \rangle^{(d)}$ are observed, resulting from the strong alignments of these pairs of vectors. There is also a clear tendency of parallel alignment of ω and $\boldsymbol{W}^c$ inside shocks. But in the expansion region downstream of the shocks, the alignment of ω and $\boldsymbol{W}^c$ changes to be anti-parallel, giving rise to the destruction of enstrophy.

D. Effect of shocklets on the strain rate tensor

We shall now address the properties of the strain rate tensor on two sides of shocks. It is well known that the vorticity tends to be aligned with the second eigenvector of strain rate tensor in a wide range of incompressible turbulent flows.[28,29] In Fig. 23, average cosines of angles between vorticity and strain rate eigenvectors on two sides of shocks are shown. Here, the index k denotes the first (most negative eigenvalue), second, and third (most positive eigenvalue) eigenvectors. The strong tendency for the vorticity to be aligned with the intermediate strain rate eigenvector and to
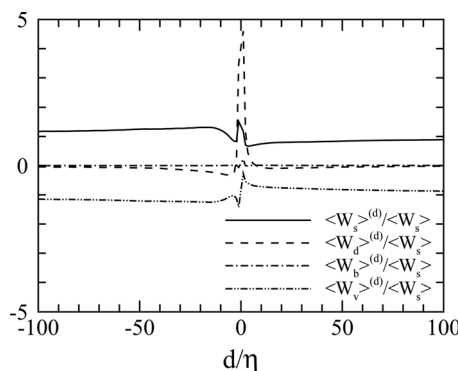
be perpendicular to the first strain rate eigenvector are both indicated in Fig. 23(a). The tendencies are somewhat weakened by shocks but are still significant. For the solenoidal component of the strain rate tensor, the orientations of its eigenvectors with vorticity are essentially not affected by the shocks (Fig. 23(b)), with average cosines of the three eigenvectors relative to the vorticity at 0.30, 0.45, and 0.69, respectively. On the other hand, the orientations of the strain rate eigenvectors of the compressive velocity component with vorticity are not as clear (Fig. 23(c)), indicating that the compressive component of the strain has little effect on the orientation of the vorticity vector.

As demonstrated in the case of vorticity, the shocks not only amplify a vorticity magnitude, but also alter its orientation. In Fig. 24, average cosines of the angles between shock normal and strain rate eigenvectors are shown. The average orientations of the strain rate eigenvectors with the shock normal direction evolve non-monotonically downstream of shocks. Inside shocks, high compression leads to a strong tendency for the first strain rate eigenvector to align with the shock normal, and the other strain rate eigenvectors perpendicular to the shock direction. Downstream of the shocks, the effects of expansion on the orientations of the strain rate eigenvectors are complicated. To facilitate the discussion of these expansion effects, we perform Helmholtz decomposition on the strain rate tensor. The average orientations of the strain rate eigenvectors of the solenoidal velocity component decrease monotonically downstream of shocks. The behaviors of the strain rate eigenvectors of the compressive

FIG. 20. Average enstrophy generation terms on two sides of the shocks, as a function of distance from the shock front.

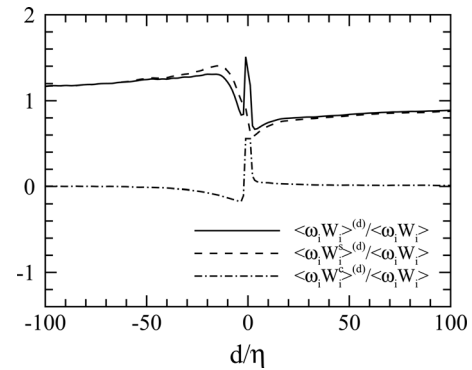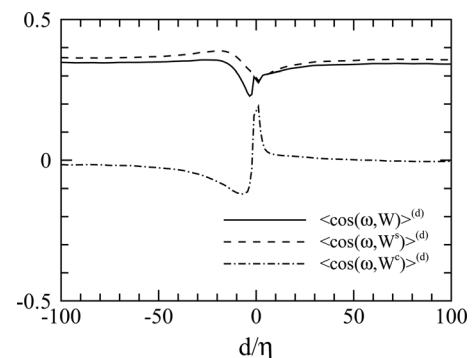FIG. 22. Average cosines of angles between vorticity and vortex stretching vectors on two sides of shocks.

FIG. 23. Average cosines of angles between vorticity and the strain rate eigenvectors on two sides of the shocks.
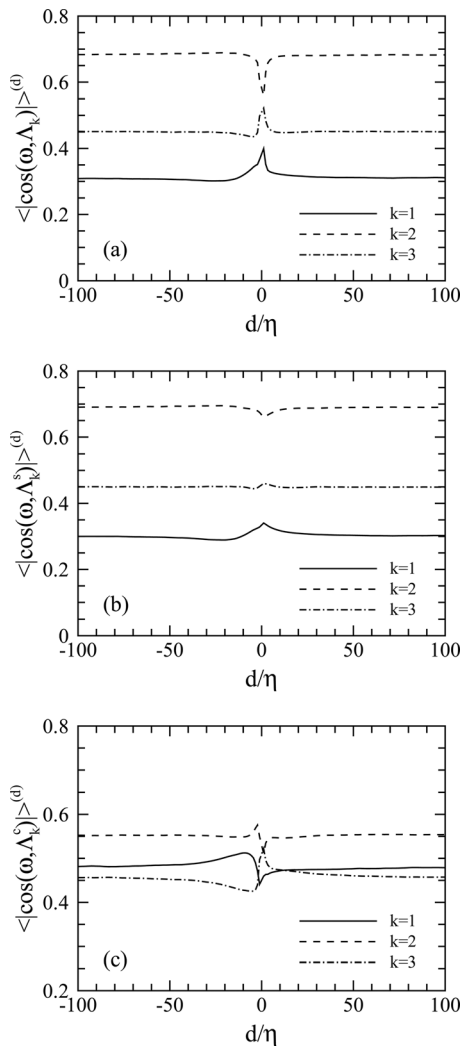
FIG. 24. Average cosines of angles between the shock normal and the strain rate eigenvectors on two sides of the shocks.

velocity component are interesting. The expansion could cause a strong tendency for the third strain rate eigenvector of the compressive velocity component to be aligned with the shock normal and other eigenvectors to be perpendicular to the shock normal. The switch between the compression region and the expansion region just downstream of the shocks leads to substantial variations of the average orientations of the strain rate eigenvectors of the compressive velocity component relative to the shock normal. The orientation of the vorticity relative to the shock normal was also plotted in Fig. 24(b) and was found to be very similar to the intermediate eigenvector of the solenoidal strain rate tensor. Thus, these two quantities are mutually compressed by the shocks and the relative geometric relation between them do not change near shocks, indicating that the process of vortex stretching by the solenoidal straining is not much affected directly by the extreme compression of shocks.

Fig. 25 shows the PDFs of cosines of angles between shock direction and the strain rate eigenvectors downstream of shocks. The parallel alignment of the first strain rate eigenvector with shock normal is observed. In addition, there is a tendency for the intermediate strain rate eigenvector to
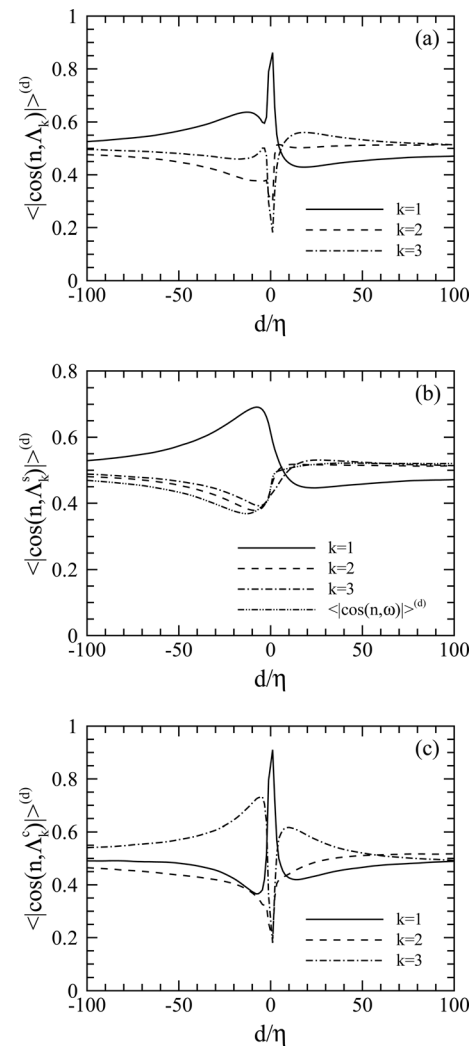
be perpendicular to the shock normal. The orientation of the third strain rate eigenvector does not seem to be affected by the shocks. These changes in alignments are weakened as the sample point moves away from the shocks but they remain visible even at $d/\eta = 72$ (i.e., k = 64).

After performing the Helmholtz decomposition on the strain rate tensor, the same tendency of the perpendicular alignment of the intermediate eigenvector relative to the shock normal is observed for each component of strain rate tensor downstream of the shocks (see Figs. 26 and 27). In contrast to the case of the total strain rate tensor, the first eigenvector of the strain rate tensor of the compressive velocity component is perpendicular to the shock normal, leading to a stronger parallel alignment of the first eigenvector of the strain rate tensor of the solenoidal velocity component with the shock normal. Furthermore, there is a very strong tendency for the third eigenvector of the strain rate tensor of the compressive velocity component to be aligned with the shock normal in the expansion region downstream of shocks. A perpendicular alignment between the third eigenvector of the solenoidal strain rate tensor with the shock normal is also observed.
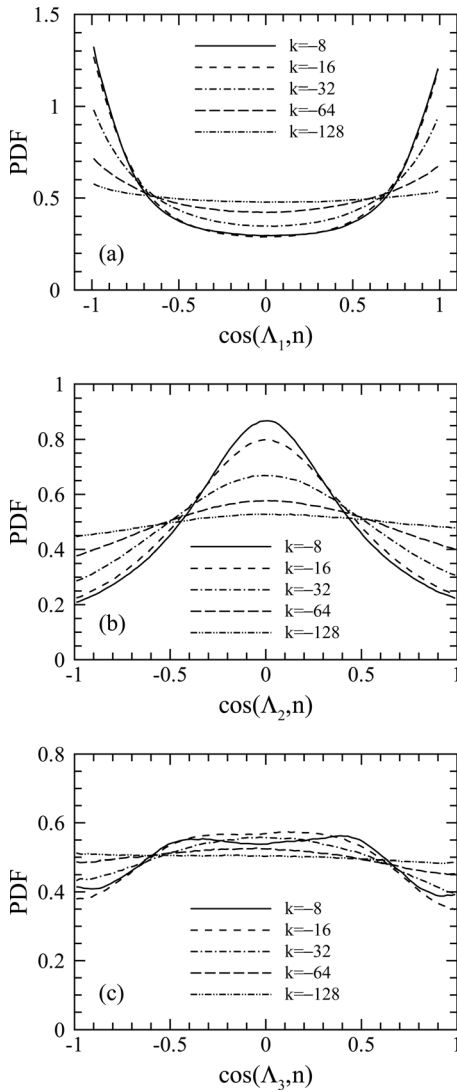
FIG. 25. PDFs of cosines of angles between the shock normal and the strain rate eigenvectors downstream of the shocks. The sample points are located k grid points away from shock and $d/\eta = 1.12\,k$.
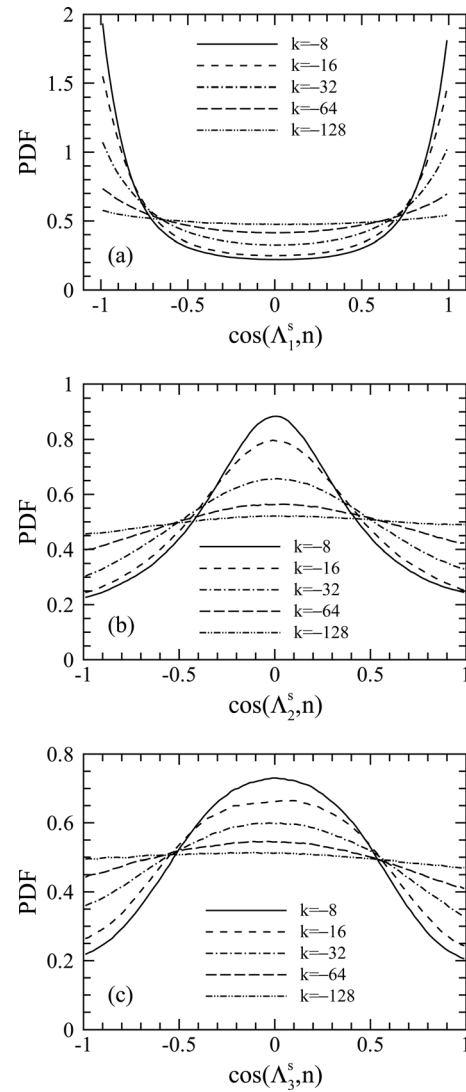

FIG. 26. PDFs of cosines of angles between the shock normal and the strain rate eigenvectors of the solenoidal velocity component downstream of the shocks. The sample points are located k grid points away from shock and $d/\eta = 1.12\,k$.

Next, we study how the three eigenvalues of the strain rate tensor are altered by the shocks. Isotropic component of the strain rate tensor has been extracted, to facilitate the comparison with the case of incompressible turbulence. Thus, the sum of three strain rate eigenvalues is always zero, i.e., $\lambda_1^* + \lambda_2^* + \lambda_3^* = 0$, where, $\lambda_1^* < \lambda_2^* < \lambda_3^*$ is assumed. The average strain rate eigenvalues on two sides of the shocks are plotted in Fig. 28. Their magnitudes are significantly amplified by the extreme compression inside shocks. The amplifications of the first and the third eigenvalues are still observable downstream of the shocks. After the Helmholtz decomposition, the average solenoidal strain rate eigenvalues change smoothly across shocks and increase slightly downstream of the shocks. For the compressive component of the stain rate tensor, the average eigenvalues exhibit sharp peaks around the shock fronts. However, at downstream locations, these average eigenvalues recover their respective upstream values.

Finally, PDFs of the ratios of the intermediate to the minimum eigenvalue of the strain rate tensor on two sides of

shocks are plotted in Fig. 29. As the sample points move closer to the shocks, the peak location of PDF shifts closer to $\lambda_2^*/\lambda_1^* = -0.5$, corresponding to the eigenvalue ratio of $-2:1:1$, implying sheet-like structures of the shock waves. After the Helmholtz decomposition, the effect of shocks on the PDFs of the eigenvalue ratios of the solenoidal strain rate tensor is negligible. However, the eigenvalue ratios of the strain rate tensor of the compressive velocity component are rather sensitive to the formation of shocks. The most probable ratio is now very close to $\lambda_2^{c*}/\lambda_1^{c*} = -0.5$, as the sheet-like structures dominate the strain rate tensor of the compressive velocity component near shocks.

IV. SUMMARY AND CONCLUSIONS

In this paper, we investigated systematically the effects of randomly generated shocks on the dynamics of velocity and velocity gradients, using a simulated compressible turbulence at turbulent Mach number of 1.03. The shock detection algorithm of Samtaney *et al.*[9] was used to extract shocks
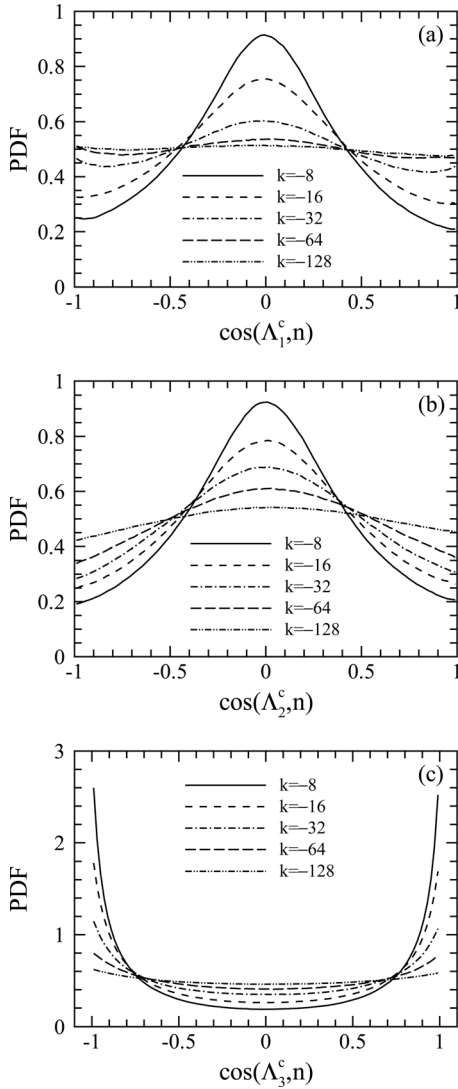
FIG. 27. PDFs of cosines of angles between the shock normal and the strain rate eigenvectors of the compressive velocity component downstream of the shocks. The sample points are located k grid points away from the shock front and $d/\eta = 1.12\,k$.

FIG. 28. Average strain rate eigenvalues on two sides of the shocks. The strain rate eigenvalues are normalized by the rms strain $S^{*\prime} = \langle S^{*2} \rangle^{1/2}$, where $S^{*} = \sqrt{S^{*}_{ij} S^{*}_{ij}}$.

from the simulated flow. Consistent with the previous finding in Samtaney *et al.*,[9] we found that the ideal normal shock relations were approximately valid across the shocks. However, we found that, for the moderate and strong shocks simulated here, the PDF of shock intensity as measured by the normal upstream shock Mach numbers exhibited an exponential tail, a feature that was different from the previous super-exponential distribution proposed for weak shocks in isotropic turbulence.

The main focus of the paper was to examine in detail the various flow properties across the shocks and how the shocks introduced both local and global changes to the small-scale flow features. Using a reference frame moving with a detected shock and performing ensemble averages over a large number of shocks, ensemble averages of various quantities on the two sides of the shocks were obtained. We found that an extended expansion region appeared downstream of the shocks. The upstream normal velocity was significantly larger than downstream normal velocity even at a distance that falls within the
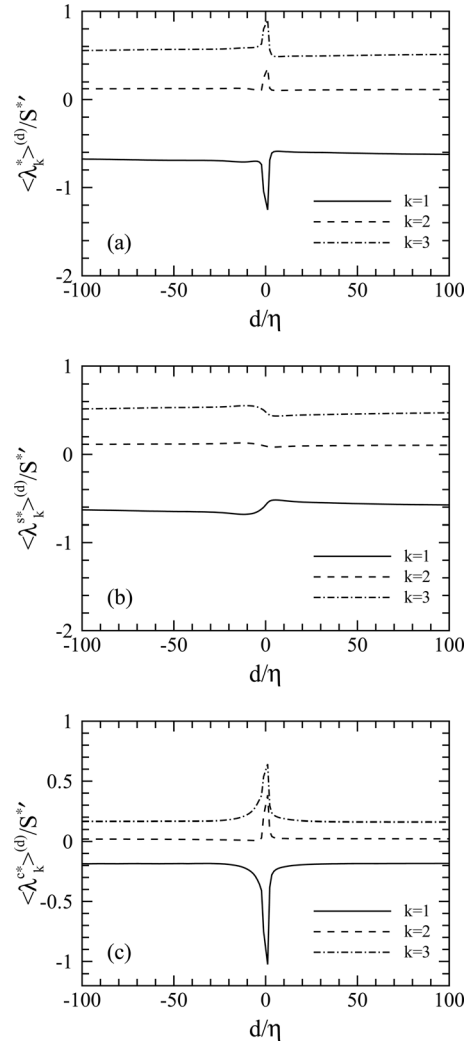
inertial subrange, implying that generation of the shocks involved a wide range of scales of the velocity field in compressible turbulence. The upstream velocity was found to have a strong tendency to be aligned with the shock normal, consistent with the local validity of ideal shock relations across the shocks. The tangential vorticity downstream of the shocks was found to be larger than that upstream of shocks due to the amplification by the shocks. In addition, we found that the downstream vorticity showed a tendency to be perpendicular to the shock normal at least in the range $-72\eta < d < 0$, implying that the correlation between vorticity and shocks extends into the inertial subrange scales.

The effect of local shock strength was also investigated by conditioned flow statistics. As a local shock grew in its strength, the average upstream normal velocity was found to increase and the average upstream tangential vorticity was found to decrease, implying that a more intense non-rotational fluid motion tends to generate a stronger shock. The statistics of downstream normal velocity and tangential vorticity were found to be insensitive to the shock strength. Local normal-shock relations were found to be increasingly more accurate with increasing shock strength, indicating that
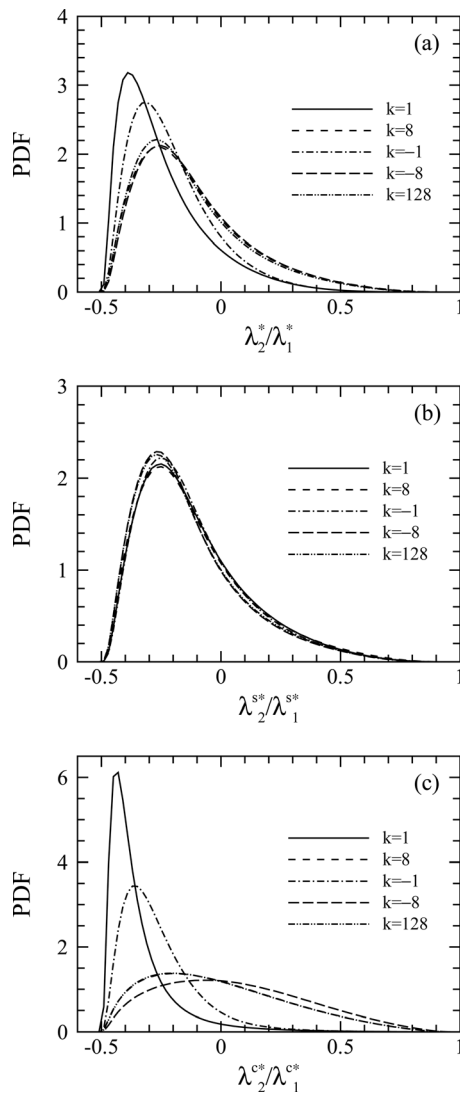
FIG. 29. PDFs of the ratios of strain rate eigenvalues on two sides of the shocks. The sample points are located k grid points away from the shock front and $d/\eta = 1.12\,k$.

the local conservations laws govern the property changes across a strong shock in the compressible turbulence.

The local enstrophy generation was also altered by the shocks. While the baroclinic effect was found to be always negligible, the compression inside the shock regions generates enstrophy locally and this additional enstrophy was not fully dissipated within the shock regions, but was partially redistributed and dissipated outside the shock regions. As in incompressible turbulence, vortex stretching dominated the enstrophy production outside the shocks.

The relative alignments of various small-scale quantities were systematically studied. The results showed that: (1) the vorticity vector was aligned parallel to the intermediate strain rate vector and perpendicular to the first strain rate vector outside shocks, similar to the case of incompressible turbulence; (2) inside shocks, similar correlations between the vorticity vector and the solenoidal strain rate eigenvectors were found; and (3) the shocks, through their effect on the compressive strain rate tensors, weakened the above correlations between vorticity and strain rate eigenvectors within the shock regions.

The orientations of the downstream strain rate eigenvectors relative to the shock normal depended on a number of factors. By applying the Helmholtz decomposition, it was found that correlations between the solenoidal component of the downstream strain rate eigenvectors and the shock normal monotonically decreased. However, there were rapid variations of the orientations of the compressive component of the downstream strain rate eigenvectors at the junction between the expansion region and compression region. Furthermore, PDFs of cosines of angles between the downstream strain rate eigenvectors and shock normal at a few selected distances from the shock front were obtained, showing that the first eigenvector tended to be parallel to the shock normal and the intermediate eigenvector tended to be perpendicular to the shock normal. The third eigenvector of the *compressive* component of the strain rate tensor showed a very strong tendency to align with the shock normal in the downstream expansion region and the third eigenvector of the *solenoidal* component of the strain rate tensor tended to be perpendicular to the shock normal there.

Finally, we showed that the strain rate eigenvalues were amplified by the compression within the shocks. Eigenvalues of the solenoidal component of the strain rate tensor changed smoothly across shocks and the corresponding eigenvalue ratio was not affected by the shocks. In contrast, the ratio of the compressive component of the strain rate eigenvalues was very sensitive to local shock compression.

In summary, the above analysis and findings show a strong effect of the randomly generated shocks in high Mach number turbulence, on the structure and dynamics of small-scale flow features. The effects of shocks and compressibility seem to extend over a wide range of scales, and their characteristics change with turbulent Mach number and flow scale separations. The Helmholtz decomposition was found to be very useful in separating out the additional effects by the shocks from the established flow features in incompressible turbulence. Furthermore, the changes of flow properties across strong shocklets could be well described by simple normal-shock relations. We believe these findings provide insights into the shock-small scale turbulence interactions. Using the improved understanding obtained here, we hope to develop a better subgrid scale modeling for highly compressible turbulence.

ACKNOWLEDGMENTS

[1]O. Zeman, "Dilatation dissipation: The concept and application in modeling compressible mixing layers," Phys. Fluids A **2**, 178 (1990).

[2]O. Zeman, "On the decay of compressible isotropic turbulence," Phys. Fluids A **3**, 951 (1991).

[3]S. Sarkar, G. Erlebacher, M. Y. Hussaini, and H. O. Kreiss, "The analysis and modelling of dilatational terms in compressible turbulence," J. Fluid Mech. **227**, 473 (1991).

[4]S. Lee, S. Lele, and P. Moin, "Eddy shocklets in decaying compressible turbulence," Phys. Fluids A **3**, 657 (1991).

[5]S. Kida and S. A. Orszag, "Enstrophy budget in decaying compressible turbulence," J. Sci. Comput. **5**, 1 (1990).

[6]J. M. Picone and J. P. Boris, "Vorticity generation by shock propagation through bubbles in a gas," J. Fluid Mech. **189**, 23 (1988).

[7]S. Kida and S. A. Orszag, "Energy and spectral dynamics in forced compressible turbulence," J. Sci. Comput. **5**, 85 (1990).

[8]S. Kida and S. A. Orszag, "Energy and spectral dynamics in decaying compressible turbulence," J. Sci. Comput. **7**, 1 (1992).

[9]R. Samtaney, D. I. Pullin, and B. Kosovic, "Direct numerical simulation of decaying compressible turbulence and shocklet statistics," Phys. Fluids **13**, 1415 (2001).

[10]S. Pirozzoli and F. Grasso, "Direct numerical simulations of isotropic compressible turbulence: Influence of compressibility on dynamics and structures," Phys. Fluids **16**, 4386 (2004).

[11]K. Lee, S. S. Girimaji, and J. Kerimo, "Effect of compressibility on turbulent velocity gradients and small-scale structure," J. Turbul. **10**, 1 (2009).

[12]S. K. Lele, "Compact finite difference schemes with spectral-like resolution," J. Comput. Phys. **103**, 16 (1992).

[13]C. W. Shu and S. Osher, "Efficient implementation of essentially non-oscillatory shock-capturing schemes," J. Comput. Phys. **77**, 439 (1988).

[14]G. S. Jiang and C. W. Shu, "Efficient implementation of weighted ENO schemes," J. Comput. Phys. **126**, 202 (1996).

[15]N. A. Adams and K. Shariff, "A high-resolution hybrid compact-ENO scheme for shock-turbulence interaction problems," J. Comput. Phys. **127**, 27 (1996).

[16]S. Pirozzoli, "Conservative hybrid compact-WENO schemes for shock-turbulence interaction," J. Comput. Phys. **178**, 81 (2002).

[17]Y. X. Ren, M. Liu, and H. Zhang, "A characteristic-wise hybrid compact-WENO scheme for solving hyperbolic conservation laws," J. Comput. Phys. **192**, 365 (2003).

[18]Q. Zhou, Z. Yao, F. He, and M. Y. Shen, "A new family of high-order compact upwind difference schemes with good spectral resolution," J. Comput. Phys. **227**, 1306 (2007).

[19]J. Larsson, A. Cook, S. K. Lele, P. Moin, B. Cabot, B. Sjogreen, H. Yee, and H. Zhong, "Computational issues and algorithm assessment for shock/turbulence interaction problems," J. Comput. Phys.: Conf. Ser. **78**, 012014 (2007).

[20]D. S. Balsara and C. W. Shu, "Monotonicity preserving weighted essentially non-oscillatory schemes with increasingly high order of accuracy," J. Comput. Phys. **160**, 405 (2000).

[21]J. Wang, L.-P. Wang, Z. Xiao, Y. Shi, and S. Chen, "A hybrid numerical simulation of isotropic compressible turbulence," J. Comput. Phys. **229**, 5257 (2010).

[22]L.-P. Wang, S. Chen, J. G. Brasseur, and J. C. Wyngaard, "Examination of hypotheses in the Kolmogorov refined turbulence theory through high-resolution simulations. Part 1. Velocity field," J. Fluid Mech. **309**, 113 (1996).

[23]Y. Andreopoulos, J. H. Agui, and G. Briassulis, "Shock wave-turbulence interactions," Annu. Rev. Fluid Mech. **32**, 309 (2000).

[24]S. Lee, S. K. Lele, and P. Moin, "Direct numerical simulation of isotropic turbulence interacting with a weak shock wave," J. Fluid Mech. **251**, 533 (1993).

[25]S. Lee, S. K. Lele, and P. Moin, "Interaction of isotropic turbulence with shock waves: Effect of shock strength," J. Fluid Mech. **340**, 225 (1997).

[26]J. Larsson and S. K. Lele, "Direct numerical simulation of canonical shock/turbulence interaction," Phys. Fluids **21**, 126101 (2009).

[27]G. Erlebacher and S. Sarkar, "Statistical analysis of the rate of strain tensor in compressible homogeneous turbulence," Phys. Fluids A **5**, 3240 (1993).

[28]W. T. Ashurst, A. R. Kerstein, R. M. Kerr, and C. H. Gibson, "Alignment of vorticity and scalar gradient with strain rate in simulated Navier-Stokes turbulence," Phys. Fluids **30**, 2343 (1987).

[29]G. E. Elsinga and I. Marusic, "Universal aspects of small-scale motions in turbulence," J. Fluid Mech. **662**, 514 (2010).